Viscoelastic flow past a confined cylinder of a low-density polyethylene melt

ELSEVIER

J. Non-Newtonian Fluid Mech., 68 (1997) 173–203

Journal of Non-Newtonian Fluid Mechanics

Viscoelastic flow past a confined cylinder of a low density polyethylene melt[1]

Frank P.T. Baaijens *, Sjaak H.A. Selen, Hans P.W. Baaijens, Gerrit W.M. Peters, Han E.H. Meijer

Centre for Polymers and Composites, Faculty of Mechanical Engineering, Eindhoven University of Technology, PO Box 513, 5600 MB, Eindhoven, The Netherlands

Received 25 January 1996; revised 20 June 1996

Abstract

The capabilities of the exponential version of the Phan-Thien–Tanner (PTT) model and the Giesekus model to predict stress fields for the viscoelastic flow of a low density polyethylene melt around a confined cylinder are investigated. Computations are based on a newly developed version of the discontinuous Galerkin method. This method gives convergent results up to a Deborah number of 2.5 for the falling sphere in a tube benchmark problem. Moreover, the specific implicit–explicit implementation allows the efficient resolution of problems with multiple relaxation times which are mandatory for polymer melts. Experimentally, stress fields are related to birefringence distributions by means of the stress optical rule. Three different fits, of equal quality, to available viscometric shear data are used: two for the PTT model and one for the Giesekus model. Comparison of computed and measured fringes reveals that neither of the models is capable of describing the full birefringence pattern sufficiently well. In particular it appears difficult to predict both the birefringent tail at the wake of the cylinder that is dominated by elongational effects and the fringe pattern between cylinder and the walls where a combined shear–elongational flow is present. © 1997 Elsevier Science B.V.

Keywords: Discontinuous Galerkin model; LDPE melts; PTT model; Viscoelastic flow

1. Introduction

This is a continued effort to investigate the performance of existing constitutive models in predicting multidimensional complex flows. Baaijens et al. [1] investigated the flow of polymer solution around a confined cylinder. Here, the same base flow is used to investigate the viscoelastic flow of a low density polyethylene (LDPE) melt.

* Corresponding author.

[1] Paper presented at the Polymer Melt Rheology Conference, University of Wales, Aberystwyth, 3–6 September 1995.

PII S0377-0257(96)01519-4

To date, rheological characterization of viscoelastic fluids has been primarily based on viscometric shear flows. Extensional flow measurements of polymer solutions are difficult to perform [2], in many cases yield inconsistent results when changing the measurement method [3], and need a careful interpretation because the flow usually is not uniform. Elongational flow measurement of polymer melts has only just become available and is limited to low strain rates (of order 1 s^{-1}). Even if both shear and extensional data are available, this may still be insufficient for a full rheological characterization because complex flows involve combined shear and elongational deformation.

For polymer solutions, it is possible to measure stresses pointwise with the rheo-optical analyser (ROA) of Fuller and Mikkelsen [4] and velocities using laser Doppler anemometry (LDA); see [1]. Stress measurement is based on flow-induced birefringence employing the empirical linear stress optical rule. Using ROA, it is fairly straightforward to measure shear stresses and the first normal stress difference independently in planar flows. For the polymer melt studied in this work, flow-induced birefringence is measured fieldwise by means of crossed polarizers, and is correlated with a norm of the shear stress and first normal stress difference only (compare for example Aldhouse et al. [5], Han and Drexler [6–8], Isayev and Upadyay [9], Kajiwara et al. [10], Kiriakidis et al. [11], Maders et al. [12], White and Baird [13], Ahmed et al. [14,15] and Beraudo [16]). LDA velocity measurements are not performed in this work.

In the literature, attention has mainly been devoted to contraction flows. However, the presence of a corner singularity still poses major difficulties for most numerical methods, while, in particular for high contraction ratios, two-dimensionality of the upstream part of the geometry proves difficult to achieve experimentally at elevated flow rates. This is because of pressure and throughput limitations. To overcome these obstacles, the flow around a cylinder has been proposed as one of the benchmark problems; see [17].

From a numerical point of view, the efficient resolution of viscoelastic flows with multiple relaxation times is a major challenge. The majority of numerical methods used to handle multiple relaxation times are based on streamline integration coupled with a Picard iteration scheme (see Dupont and Crochet [18], Luo and Mitsoulis [19] and Hulsen and van der Zanden [20]), while Baaijens [21] used an operator splitting method. Other methods, such as the elastic–viscous stress split method introduced by Rajagopalan et al. [22], use a continuous interpolation of the extra stress tensor leading to a unmanageably large number of unknowns in the case of multiple relaxation times. Here, a modification of the discontinuous Galerkin (DG) method, first introduced by Fortin and Fortin [23], is applied. The stability of this formulation is significantly enhanced by introducing the modified elastic viscous stress split method proposed by Guénette and Fortin [24]. The current DG method allows the use of a bilinear stress interpolation on a quadratic velocity element, thereby greatly improving the efficiency compared with the quadratic stress interpolation applied by Baaijens et al. [25]. Accuracy and stability of this enhanced DG method are demonstrated for the falling sphere in a tube benchmark problem employing the upper convected Maxwell (UCM) model. Furthermore, by using the implicit–explicit implementation proposed previously by Baaijens [26] all extra stress variables can be eliminated on the element level, yielding a cost-effective method: computing cost is approximately linearly proportional to the number of relaxation times.

The predictive capabilities of two constitutive models are investigated: the exponential version of the Phan-Thien–Tanner (PTT) model and the Giesekus model. All material parameters are

fitted on steady shear data only. Primarily a four-mode fit is used, while comparison with a one-mode and an eight-mode fit is also performed. Furthermore, the sensitivity of the predicted fringe patterns with respect to the non-linear parameters in the constitutive models is investigated.

The outline of this paper is as follows. First, the mathematical formulation of the problem is presented together with the definition of the constitutive models. Thereafter, the enhancement of the DG method is introduced and the performance of this enhancement for the falling sphere in a tube benchmark problem is explored. Next, the rheological characterization of the LDPE melt is presented together with the experimental set-up. Finally, a comparison between predicted and computed isochromatic fringes is made, from which conclusions are drawn.

2. Problem definition

Consider the inertia-less, isothermal, incompressible flow governed by

$$\nabla\cdot(-p\mathbf{I}+\boldsymbol{\tau})=\mathbf{0}, \tag{1}$$

$$\nabla\cdot\boldsymbol{u}=0, \tag{2}$$

where p denotes the pressure, $\boldsymbol{\tau}$ the extra stress tensor, $\boldsymbol{u}$ the velocity field and ∇ the gradient operator.

In this work multimode constitutive models are applied for the extra stress tensor $\boldsymbol{\tau}$, giving

$$\boldsymbol{\tau}=2\eta_s\boldsymbol{D}+\sum_{i=1}^{N}\boldsymbol{\tau}_i, \tag{3}$$

where η_s denotes the viscosity of a purely viscous contribution, $\boldsymbol{D}$ the rate of deformation tensor ($\boldsymbol{D}=\frac{1}{2}(\nabla\boldsymbol{u}+(\nabla\boldsymbol{u})^{\mathrm{T}})$, and $\boldsymbol{\tau}_i$ the contribution of the ith relaxation time. The constitutive models used are of the differential type and have the following generic form

$$\lambda_i\overset{\square}{\boldsymbol{\tau}}_i+\boldsymbol{Y}_i\cdot\boldsymbol{\tau}_i=2\eta_i\boldsymbol{D}, \tag{4}$$

with λ_i and η_i the ith relaxation time and viscosity respectively, while the objective derivative $\overset{\square}{\boldsymbol{\tau}}$ is defined by

$$\overset{\square}{\boldsymbol{\tau}}=\frac{\partial\boldsymbol{\tau}}{\partial t}+\boldsymbol{u}\cdot\nabla\boldsymbol{\tau}-(\boldsymbol{L}-\xi\boldsymbol{D})\cdot\boldsymbol{\tau}-\boldsymbol{\tau}\cdot(\boldsymbol{L}-\xi\boldsymbol{D})^{\mathrm{T}}, \tag{5}$$

where $\boldsymbol{L}=\nabla\boldsymbol{u}$. For the tensor $\boldsymbol{Y}$ two alternatives are investigated: one yields the exponential PTT model commonly used for polymer melts, i.e.

$$\boldsymbol{Y}=\exp\left[\frac{\varepsilon\lambda}{\eta}\,\mathrm{tr}(\boldsymbol{\tau})\right]\mathbf{I}, \tag{6}$$

and the other gives the Giesekus model:

$$\boldsymbol{Y}=\mathbf{I}+\frac{\alpha\lambda}{\lambda}\boldsymbol{\tau}. \tag{7}$$

The UCM model is recovered by selecting $\xi = 0$ and $\boldsymbol{Y} = \mathbf{I}$.

Along the input boundary fully developed flow is assumed and both the velocities and extra stresses are prescribed.

3. Stabilized discontinuous Galerkin method

One of the key problems in mixed stress–velocity–pressure formulations is the selection of the discretization spaces for these variables with respect to each other. To have compatibility between velocities and stresses, Marchal and Crochet [27] introduced an $n \times n$-bilinear subdivision of the extra stress variable in combination with a biquadratic interpolation of the velocity. To circumvent this costly subdivision, Guénette and Fortin [24] recently proposed a new mixed formulation for computing viscoelastic flows by introducing an L_2 projection of the rate of deformation tensor in combination with a stabilizing term in the discrete momentum equation. Effectively this approach can be viewed as a modification of the elastic viscous stress splitting scheme proposed by Rajagopalan et al. [22]. Guénette and Fortin [24] showed that this allowed for a continuous bilinear interpolation of the extra stress and rate of deformation tensor when using a biquadratic velocity field.

In this work, the same methodology is investigated but with discontinuous interpolations of the extra stress tensor, as used in the DG method (see Fortin and Fortin [23] and Baaijens [26–28]).

Define $\mathscr{L}\tau$ as

$$\mathscr{L}\tau = \lambda[\boldsymbol{u}\cdot\nabla\tau - (\boldsymbol{L}\cdot - \xi\boldsymbol{D})\,\tau - \tau\cdot(\boldsymbol{L}^{\mathrm{T}} - \xi\boldsymbol{D})] + \boldsymbol{Y}\cdot\tau. \tag{8}$$

Application of the DG method in combination with an L_2 projection of the rate of deformation tensor, as introduced by Guénette and Fortin [24], and the use of the implicit–explicit time discretization proposed by Baaijens [26], gives the following.

Problem 1 (DG–SE). Given $\tau_{i_n} = \tau_i(t = t_n)$, find $(\tau_i, \boldsymbol{u}, p, \boldsymbol{D})$ at $t = t_n + \Delta t$ such that for all admissible $(\boldsymbol{s}_i, \boldsymbol{v}, q, \boldsymbol{e})$

$$\left(\boldsymbol{s}_i, \lambda\frac{\tau_i - \tau_{i_n}}{\Delta t} + \mathscr{L}\tau_i - 2\eta\boldsymbol{D}_{\boldsymbol{u}}\right) - \sum_{e=1}^{N_{\mathrm{el}}}\int_{\Gamma^e_{\mathrm{in}}}\boldsymbol{s}_i{:}\boldsymbol{u}\cdot\boldsymbol{n}\lambda(\tau_i - \tau_{i_n}^{\mathrm{ext}})\,\mathrm{d}\Gamma = 0, \quad i = 1, 2, 3,\ldots, \tag{9}$$

$$-\left(\boldsymbol{D}_{\boldsymbol{v}}, 2\eta_{\mathrm{s}}\boldsymbol{D}_{\boldsymbol{u}} + 2\bar{\eta}(\boldsymbol{D}_{\boldsymbol{u}} - \bar{\boldsymbol{D}}) + \sum_{i=1}^{N}\tau_i\right) + (\nabla\cdot\boldsymbol{v}, p) = 0, \tag{10}$$

$$(\boldsymbol{e}, \boldsymbol{D}_{\boldsymbol{u}} - \bar{\boldsymbol{D}}) = 0, \tag{11}$$

$$(q, \nabla\cdot\boldsymbol{u}) = 0. \tag{12}$$

In this, $(\cdot,\cdot)$ denotes the appropriate inner product on the domain Ω, Γ^e_{in} is the inflow boundary of element Ω^e, $\boldsymbol{n}$ the unit outward normal to Γ^e, τ^{ext} the stress tensor of the neighbouring, upwind, element, $\boldsymbol{D}_{\boldsymbol{u}} = \boldsymbol{D}(\boldsymbol{u})$, $\boldsymbol{D}_{\boldsymbol{v}} = \boldsymbol{D}(\boldsymbol{v})$, and finally $\bar{\eta}$ a yet to be specified auxiliary viscosity.

Notice that the discrete rate of deformation tensor $\bar{\boldsymbol{D}}$ is only used as a stabilization factor in the discrete equilibrium Eq. (10). It is not introduced in the stress Eq. (9). This formulation is

a direct generalization of the method proposed by Guénette and Fortin [24]. An alternative to the above is to replace $\boldsymbol{D}_u$ in Eq. (9) by the discrete approximation $\bar{\boldsymbol{D}}$. However, numerical experiments revealed negligible effects of this replacement. A third option is to perform an L_2 projection of the velocity gradient tensor $\boldsymbol{L}$, yielding $\bar{\boldsymbol{L}}$. In analogy with the EVSS-G formulation introduced by Szady et al. [29] this discrete $\bar{\boldsymbol{L}}$ may also be inserted in the weak form of the constitutive equation, notably in the definition of the operator $\mathscr{L}\tau$, while $\boldsymbol{D}_u$ may be replaced by $\frac{1}{2}(\bar{\boldsymbol{L}}+\bar{\boldsymbol{L}}^{\mathrm{T}})$. Again, numerical experiments revealed no improvement over the DG–SE formulation described above.

The resulting set of non-linear equations is solved using a one-step Newton iteration scheme: only one Newton-iteration is performed at each time step. Because of the explicit approximation of τ^{ext} the extra stresses can be eliminated on the element level. This makes this procedure rather attractive for multimode computations, because in the resulting set of linearized equations only velocity and pressure appear as unknowns; see [26] for details.

3.1. Stokes flow

In this section, the performance of the DG–SE formulation for Stokes flow conditions is investigated numerically. Stokes flow is recovered by choosing only a single relaxation time with $\lambda = 0$. Guénette and Fortin [24] have shown that a continuous bilinear interpolation of $\bar{\boldsymbol{D}}$ and τ, in combination with a biquadratic interpolation of $\boldsymbol{u}$, gives stable results. Here the effect of choosing a biquadratic velocity field and several discontinuous and continuous interpolations of $\bar{\boldsymbol{D}}$ and τ is investigated. In all cases the pressure is interpolated discontinuously with a linear function. To access the stability, the radial velocity field for the flow through an axisymmetric 4:1 contraction is compared for several interpolations and choices of the auxiliary viscosity $\bar{\eta}$.

The elements that have been tested are defined as follows. Let Ω^e denote the domain of element e and $P_k(\Omega^e)$ and $Q_k(\Omega^e)$ the kth-order interpolation polynomial on a triangular or quadrilateral element e respectively. Further, $()^{\mathrm{d}}$ denotes a discontinuous discretization over the element interfaces. In a more generalized sense, P_1 represents linear, P_2 quadratic etc. discretization, while a Q_k discretization contains no higher-order terms than strictly implied by the order k. The base discretization for the velocity–pressure is $(\boldsymbol{u}, p) \rightarrow Q_2P_1^{\mathrm{d}}$. The extra stress tensor is interpolated constant (Q_0^{d}), bilinear (Q_1^{d}) or biquadratic (Q_2^{d}), in all cases discontinuously from element to element. Equal-order interpolation of the discrete rate of deformation tensor $\bar{\boldsymbol{D}}$ is chosen. In the case of the bilinear interpolation, both a continuous and a discontinuous interpolation of $\bar{\boldsymbol{D}}$ are investigated. Thus the elements that have been tested are $(\tau, \boldsymbol{u}, p, \bar{\boldsymbol{D}}) \rightarrow$ $(Q_0^{\mathrm{d}}Q_2P_1^{\mathrm{d}}Q_0^{\mathrm{d}})$, $(Q_1^{\mathrm{d}}Q_2P_1^{d}Q_1^{\mathrm{d}})$, $(Q_2^{\mathrm{d}}Q_2P_1^{\mathrm{d}}Q_2^{\mathrm{d}})$, and $(Q_1^{\mathrm{d}}Q_2P_1^{\mathrm{d}}Q_2)$.

The base mesh is shown in Fig. 1. On the inflow boundary a fully developed velocity profile is prescribed, while at the outflow boundary the radial velocity is suppressed.

The auxiliary viscosity $\bar{\eta}$ is chosen as $\bar{\eta} = \beta\eta$. In addition to the cases $\beta = 0$ and $\beta = 1$, a sensitivity analysis with respect to the choice of β is made.

For $\beta = 0$, Fig. 2 shows contours of the radial velocity. Fig. 2(a)–(c) correspond to a constant, bilinear and biquadratic interpolation respectively of the extra stress tensor. In all parts of the figure the same eight contour levels between the minimum and maximum value are depicted. For the constant stress elements (Fig. 2(a)) a nearly singular coefficient matrix is obtained and, consequently, the velocity field exhibits tremendous oscillations. For the bilinear

stress element (Fig. 2(b)) the radial velocity field exhibits small oscillations, reflecting a near compatibility between stress and velocity interpolation. The biquadratic element of Fig. 2(c) displays a good compatibility as no oscillations are visible.

For $\beta = 1$, Fig. 3(a)–(c) shows the same results as in Fig. 2, while Fig. 3(d) shows the results for the case where the discrete rate of deformation $\bar{\boldsymbol{D}}$ is the interpolated with a continuous bilinear polynomial. Now, all interpolations tested exhibit smooth radial velocity profiles that are in good agreement with each other. The oscillations of the bilinear element have vanished, while, remarkably, the constant stress element also produces smooth results. The latter is interesting, in view of the results of Baaijens [26], for handling singularities in the flow domain.

Finally, the effect of varying the adjustable parameter β is investigated for the element $(\boldsymbol{\tau}, \boldsymbol{u}, p, \bar{\boldsymbol{D}}) \rightarrow (Q_1^d Q_2 P_1^d Q_1)$. Fig. 4 shows for $\beta = 0.01$, 0.1, 10 and 100 the radial velocity profile as before for the bilinear stress element of the DG–SE formulation. For $\beta = 0.01$ some small oscillations may be observed, while smooth results are obtained for all other values. This demonstrates the robustness of the stabilization procedure which is relatively insensitive to the choice of β in the Stokes flow case.

3.2. Viscoelastic flow

From the elements tested in the previous section, the constant and bilinear stress elements appear to be the most attractive for viscoelastic flow calculations. Based on the results of Baaijens [28], the constant stress element is expected to give stable results up to high values of the Deborah number, but yields an algorithm of order h only. The linear stress element, on the contrary, yields an algorithm of order h^2 with respect to the stresses, but may be less stable than the constant stress element as it does not satisfy the monotonicity requirements set forth in [26]. Compared with higher-order interpolations, the bilinear stress element is much more economic

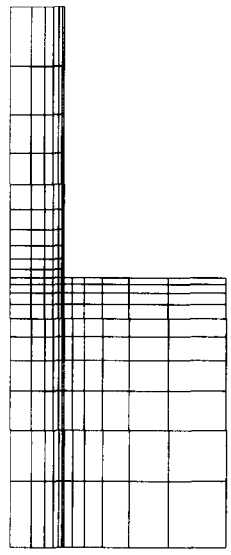

Fig. 1. Mesh used for axi-symmetric 4:1 contraction problem.

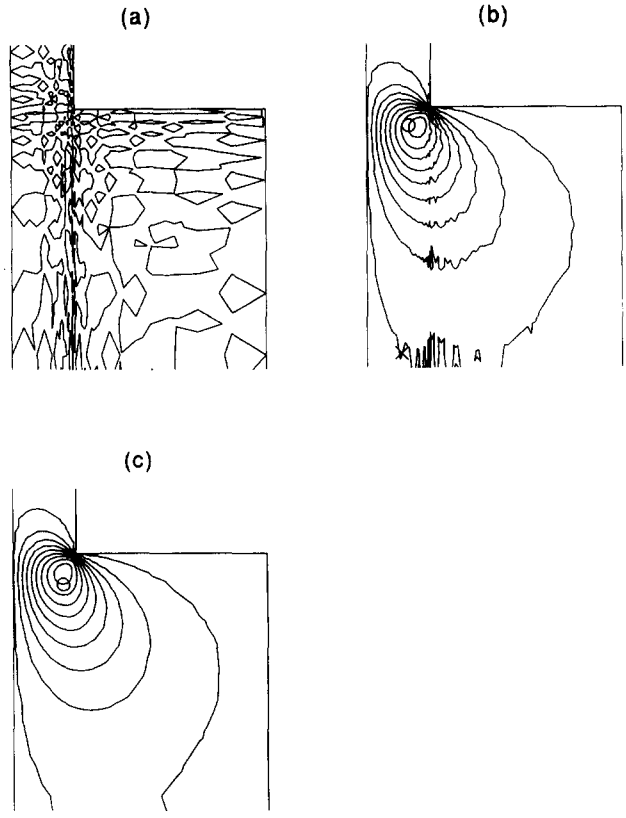

Fig. 2. Radial velocity field for various stress interpolations for $\beta = 0$: (a) Q_0^d; (b) Q_1^d; (c) Q_2^d.

while being sufficiently accurate. In fact, the bilinear stress element produced more stable results than the biquadratic element.

To test the performance of the proposed numerical scheme for viscoelastic flow analysis, the falling sphere in a tube benchmark problem is investigated.

The sphere is located at the centre-line of the tube, as depicted in Fig. 5. The tube wall moves parallel to the centre-line with a velocity V in the positive z-direction. The ratio B_c/R of the cylinder radius R_c and the sphere radius R is 2. The Deborah number is defined as

$$De = \frac{\lambda V}{R}. \tag{13}$$

The drag F_0 on a sphere falling in an unbounded newtonian medium is given by

$$F_0 = 6\pi\eta RV. \tag{14}$$

It is customary to compare the so-called drag correction factor given by

$$K(De) = \frac{F(De)}{F_0}, \tag{15}$$

where F is the drag on the cylinder for the viscoelastic case as a function of the Deborah number.

For the analysis of the falling sphere benchmark problem four meshes are used. Meshes M1–M3 have an upstream length of $12R$ and a downstream length of $18R$. Mesh M4 also has an upstream length of $12R$, but a downstream length of $30R$. The section of the meshes near the sphere is depicted in Fig. 6, and in Table 1 some data concerning the meshes are given. Mesh refinement is only uniform from mesh M1 to M2 and M3.

Two situations are reported on in detail here: the case $\beta = 0$, giving the so-called DG–E formulation presented previously in [26], and the case $\beta = 1$ giving the DG–SE method proposed here. For $\beta = 0$, the best results are obtained with the biquadratic stress element: $(\tau, \boldsymbol{u}, p) \rightarrow (Q_2^d Q_2 P_1^d)$. For $\beta = 1$ numerical experiments showed that the most stable results are obtained by using a bilinear discontinuous interpolation of the extra stress tensor and a bilinear, but continuous, interpolation of the discrete rate of deformation tensor $\bar{\boldsymbol{D}}$ hence $(\tau, \boldsymbol{u}, p, \bar{\boldsymbol{D}}) \rightarrow (Q_1^d Q_2 P_1^d Q_1)$. Results of other interpolation schemes will be discussed later.

Table 2 and Fig. 7 compare the computed drag correction factors of both the DG–SE and the DG–E methods with the results of Lunsmann et al. [30] and Fan and Crochet [31]. Fan and Crochet [31] obtained convergence up to a Deborah number of 2 using a high-order spectral

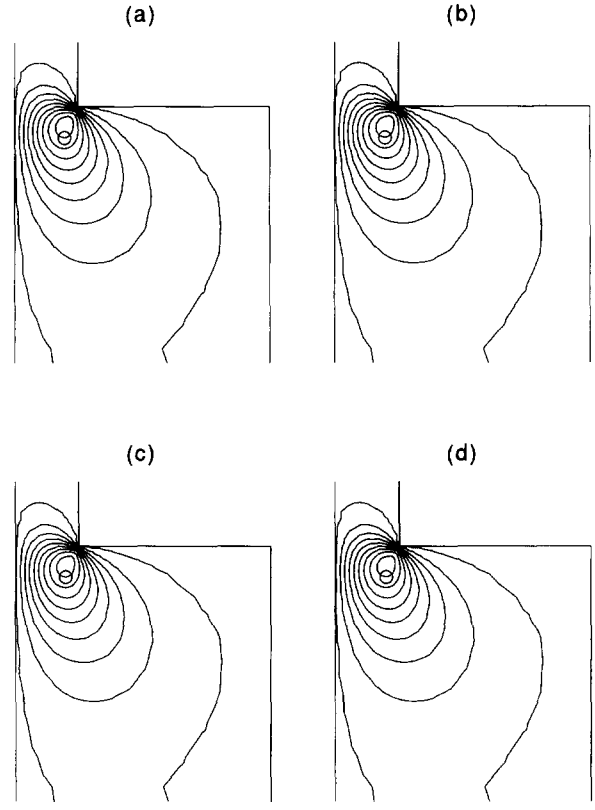

Fig. 3. Radial velocity field for various stress interpolations for $\beta = 1$: (a) Q_0^d; (b) Q_1^d; (c) Q_2^d; (d) $(\tau, \bar{\boldsymbol{D}})$:$(Q_1^d, Q_1)$.

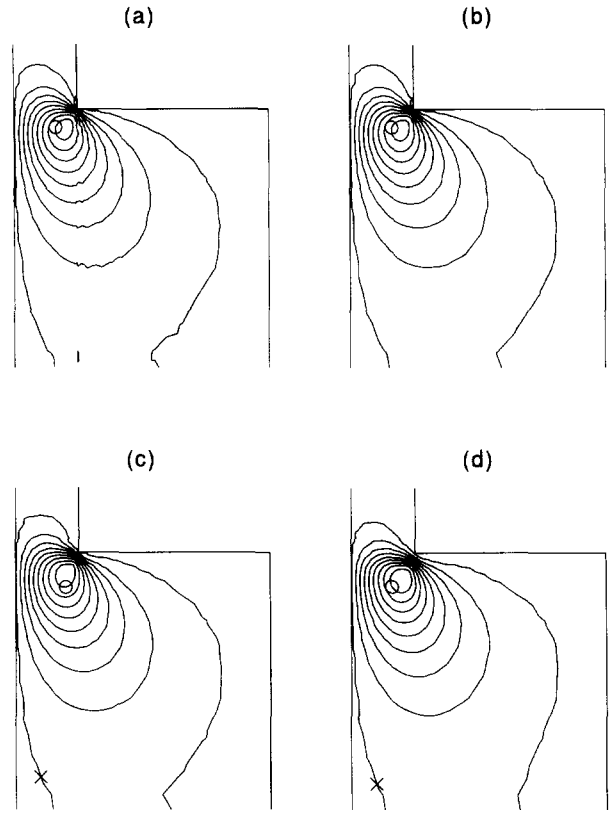

Fig. 4. Radial velocity field for various stress interpolations for (a) $\beta = 0.01$, (b) $\beta = 0.1$, (c) $\beta = 10$ and (d) $\beta = 100$.

finite element method based on the EVSS formulation, while Arigo et al. [32] obtained convergence up to $De = 2.2$ using a quadratic element and the EVSS method. However, the upswing in the drag correction curve of Arigo et al. [32] is not found here. For $De < 2$, the time step was set to $0.1 V/De\ R$ and the Deborah number is increased by 0.1, while for $De > 2$ both the time step and the increment in Deborah number were decreased by a factor of 2.

The computations demonstrate convergence with mesh refinement and are in good agreement with the results from the literature (concerning the dimensionless drag coefficient). Beyond a Deborah number of about 2.2, the results for meshes M3 and M4 deviate by about 0.1% and hence full convergence with mesh refinement has not been achieved yet. Clearly, stabilizing the DG method is a significant improvement.

To access the characteristics of the solution, Fig. 8 shows contour lines of the four extra stress components τ_{rr}, τ_{zz}, τ_{rz} and $\tau_{\phi\phi}$ at $De = 2.4$ for mesh M4. Stresses have been made dimensionless with $\eta V/R$. For all stress components, a smooth spatial distribution is found with steep gradients near the sphere surface. The τ_{zz} component develops a long tail that extends about 10 radii downstream.

The impact of the stabilization of the DG method can be seen in Fig. 9. At $De = 0.8$ and mesh M4, this figure shows the τ_{rz} component along the sphere surface and the axial velocity along the

centre-line in the wake of the cylinder. In the top two plots, the standard DG method is used with the $(Q_2^dQ_2P_1^d)$ element. The velocity profile is smooth, but significant oscillations in the stress field are observed. In the middle two plots, a bilinear stress element $(Q_1^dQ_2P_1^d)$ is used for the DG method. Now, the stress field is smooth, but oscillations in the velocity field are observed. This is consistent with the results for the Stokes flow. In the bottom two plots, the stabilized DG method is used: now both velocities and stresses are smooth. In this case the $(\tau, \boldsymbol{u}, p, \bar{\boldsymbol{D}}) \rightarrow (Q_1^dQ_2P_1^dQ_1)$ element is applied. Notice that convergence of the results with respect to the drag correction factor does not necessarily imply that a smooth stress field is obtained: the drag correction factor for the DG–E formulation at $De = 0.8$ is in good agreement with results of Lunsmann et al. [30] and Fan and Crochet [31]. Therefore, to benchmark results, it is more appropriate to use stresses along the sphere surface and the axial symmetry line than the drag correction factor.

Although the choice $\beta = 1$, or equivalently setting the auxiliary viscosity $\bar{\eta}$ equal to the viscosity η, is optimal for Stokes flow, it need not be the most appropriate choice for viscoelastic calculations. The apparent viscosity

$$\eta_a = \frac{\|\tau\|}{\|\boldsymbol{D}\|}, \quad \|\tau\| = (\tau{:}\tau)^{1/2}, \quad \|\boldsymbol{D}\| = (\boldsymbol{D}{:}\boldsymbol{D})^{1/2}, \tag{16}$$

may exceed η by several orders of magnitude which suggests that the optimal choice of the auxiliary viscosity $\bar{\eta}$ needs further investigation.

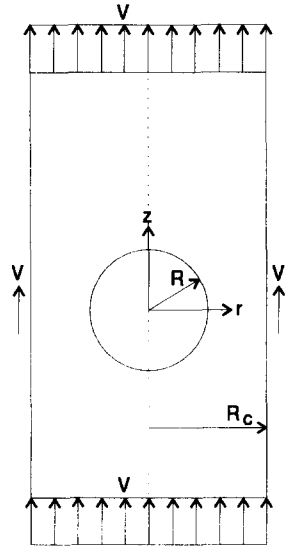

Fig. 5. Falling sphere in a tube benchmark problem.

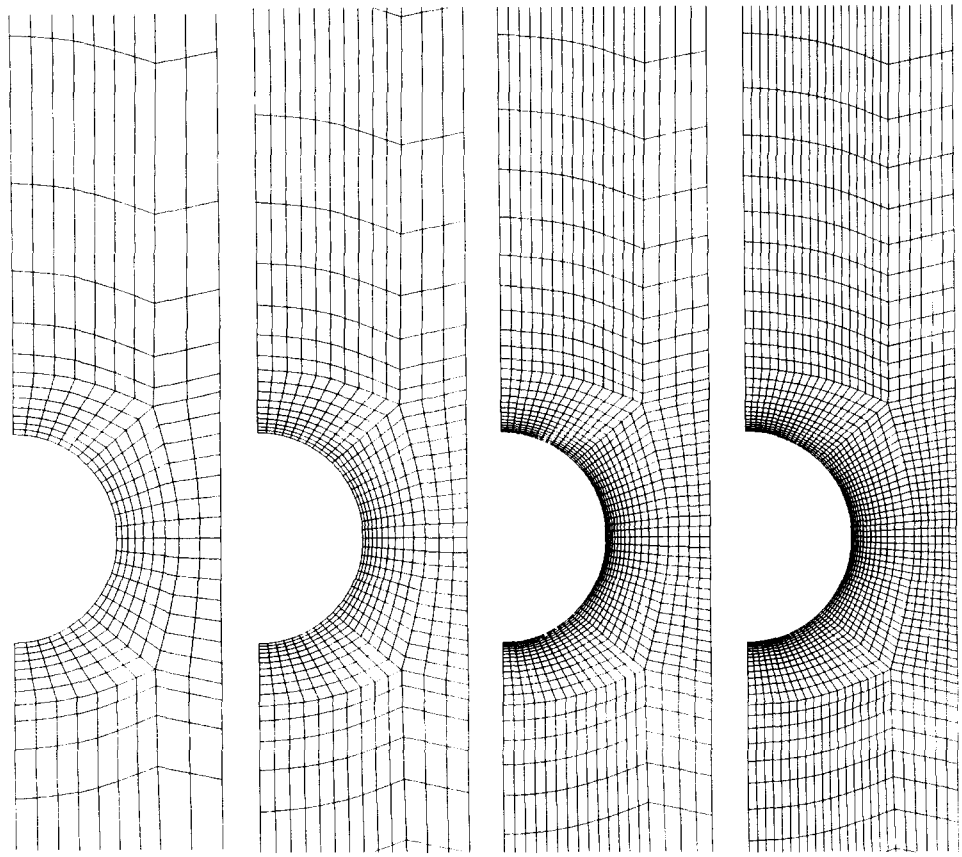

Fig. 6. Meshes used for the analysis of the falling sphere test, from left to right: M1, M2, M3, M4.

4. Experimental aspects

4.1. Flow loop

The flow cell, Fig. 10, is fed with the LDPE melt by a corotational twin screw extruder (Werner and Pfleiderer ZSK25). During all experiments, the melt temperature was controlled at 190°C.

The flow cell is made of steel (100 MnCrW4) and four changeable windows in the lateral walls, two on each side, that are made of Schott BK7 glass (Schott Glass) and have radius 50 mm and thickness 15 mm. The height of the channel is 5 mm and the depth in the neutral direction is 40 mm, giving an aspect ratio of 1:8. This ratio is assumed to be sufficiently large to create a nominally two-dimensional flow and small enough to yield relatively high Deborah numbers given the maximum flow rate achievable with the current extruder and the minimal diameter of the cylinder. The length of the channel in the mean flow direction is 320 mm.

Table 1
Characteristics of the meshes used for analysis of the falling sphere problem

Mesh	Number of elements	Number of nodes	Number of degrees of freedom	
			DG–SE	DG–E
M1	359	1541	4318	3082
M2	733	3081	8586	6162
M3	1436	5953	16529	11906
M4	2256	9295	25766	18590

The cylinder is composed of tungsten with radius $R = 1.25$ mm and is placed in blind holes in two opposite windows. To avoid damage due to contact between the cylinder and the glass, Teflon was placed between the rounded ends of the cylinder and glass. In the case when the cylinder is placed asymmetrically between the parallel plates, the cylinder is positioned $0.3R$ towards the upper wall. For the symmetrically placed cylinder the flow domain is schematically drawn in Fig. 11.

The flow cell is heated with eight heating elements (Hasco Z110, 400 W) that are located in pairs directly under and above the slit and near the entrance and exit of the flow cell. These elements are controlled by a four-channel temperature control unit (Hasco Z1295/5) that is located between two elements in the walls of the flow cell. Isothermal flow conditions are assumed throughout.

Table 2
Drag correction factor as a function of the Deborah number comparing DG–E method and DG–SE method using meshes M1–M4 with the results of Lunsmann et al. [30] and Fan and Crochet [31]

De	Lunsmann et al.	Fan and Crochet	DG–E				DG–SE			
			M1	M2	M3	M4	M1	M2	M3	M4
0.0	5.947		5.948	5.947	5.947	5.947	5.948	5.947	5.947	5.947
0.2	5.658		5.660	5.660	5.662	5.663	5.660	5.660	5.660	5.660
0.4	5.185		5.187	5.187	5.186	5.187	5.186	5.186	5.186	5.186
0.6	4.788		4.802	4.802	4.798	4.798	4.801	4.801	4.801	4.801
0.8	4.524		4.530	4.530	4.522	4.522	4.529	4.528	4.528	4.528
1.0	4.336	4.339	4.346	4.343	4.334	4.335	4.345	4.342	4.341	4.341
1.1				4.274	4.268		4.277	4.274	4.272	4.272
1.2	4.212						4.223	4.218	4.216	4.216
1.4	4.133						4.146	4.138	4.135	4.134
1.6	4.089	4.080					4.103	4.089	4.085	4.084
1.8								4.064	4.058	4.057
2.0		4.042						4.056	4.049	4.048
2.2								4.061	4.052	4.049
2.4									4.065	4.061
2.5									4.075	4.070
2.6									4.087	
2.7									4.104	

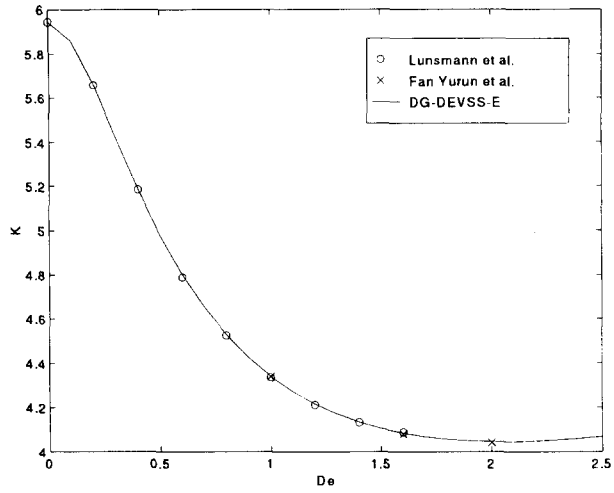

Fig. 7. Drag correction factor K as function of the Deborah number DG–SE method: mesh M4.

4.2. Birefringence measurements

Fieldwise measurement of birefringence is a classical method for studying birefringence distributions in solids [33], polymer melts and highly birefringent solutions [34]. The stress optical rule enables the interpretation of birefringence data in terms of stresses. Fuller [35] describes numerous systems for birefringence measurements. Details may also be found in the book of Azzam and Bashara [36].

In principle, both the extinction angle and the retardance can be measured in a two-step procedure, from which the shear stress τ_{xy} and the first normal stress difference N_1 can be obtained. In this work, birefringence Δn is measured only and can be related to stresses by

$$\Delta n = C(4\tau_{xy}^2 + N_1^2)^{1/2}, \tag{17}$$

with C the stress optical coefficient. In the experiments monochromatic light is used yielding isochromatic lines on a singly coloured background. These isochromatic lines correspond to the stress state according to

$$(4\tau_{xy}^2 + N_1^2)^{1/2} = \frac{k\lambda_0}{dC}, \quad k = 1, 2, 3, \ldots, \tag{18}$$

with λ_0 the wavelength of the light, d the width of the channel and C the stress optical coefficient.

The optical elements used in the experiments are listed in Table 3. All elements are mounted in line on an optical rail (Melles Griot 07ORN009). The fringe patterns are observed through a microscope (Olympus SZ4045TR) with a 1.6710 magnification.

5. Rheological characterization

The LDPE melt is a commercial grade Stamylan LD 2008XC43 (DSM), for which some characteristics are listed in Table 4. Tas [37] has performed an extensive rheological characterization in simple shear flow and in both uniaxial and biaxial extensional flow. Four non-linear viscoelastic constitutive equations were fitted (Leonov, Wagner, PTT and Giesekus) with eight relaxation times. The result was that both the Giesekus and the PTT models fitted the data fairly well. Only the relaxation of the first normal stress difference after cessation of steady shear flow distinguished between these two models, of which the PTT model agreed the closest with the experimental data. It appeared necessary to introduce the parameter ξ in the PTT model to obtain optimal agreement with data in simple shear flow and elongational flow simultaneously.

In this work, both a four-mode and an eight-mode fit are applied. The Maxwell parameters $\{\lambda_i, \eta_i\}$ are given in Table 5. The non-linear parameters are fitted to steady shear data. For the PTT model, two sets have been obtained, one with $\xi = 0$ and one with a non-zero ξ parameter,

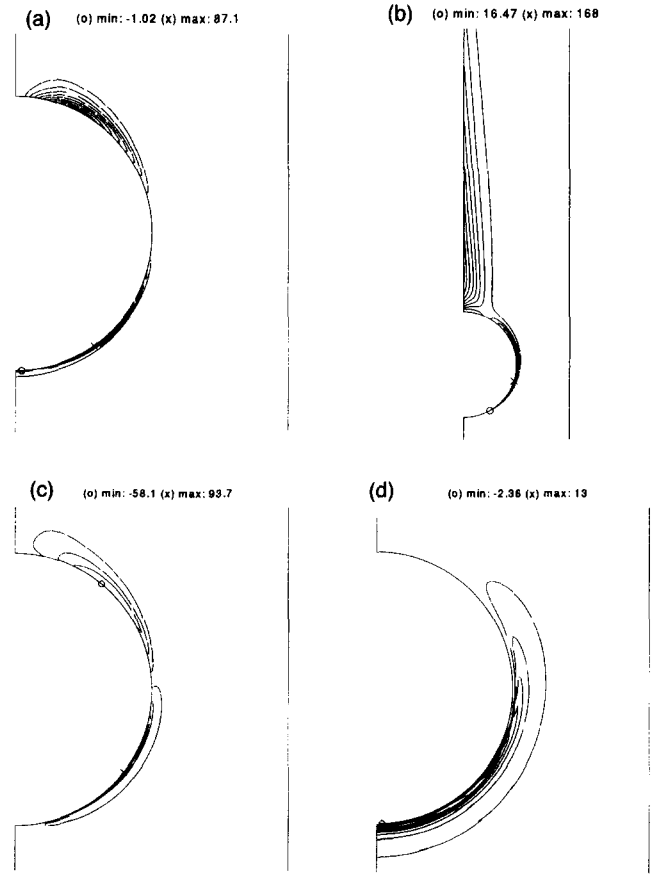

Fig. 8. Computed contour plots of discontinuous extra stress components for a falling sphere in a tube (UCM) model, De = 2.4, mesh M4, numerical method, DG–SE: (a) τ_{rr} (b) τ_{zz}; (c) τ_{rz} (d) $\tau_{\varphi\varphi}$.

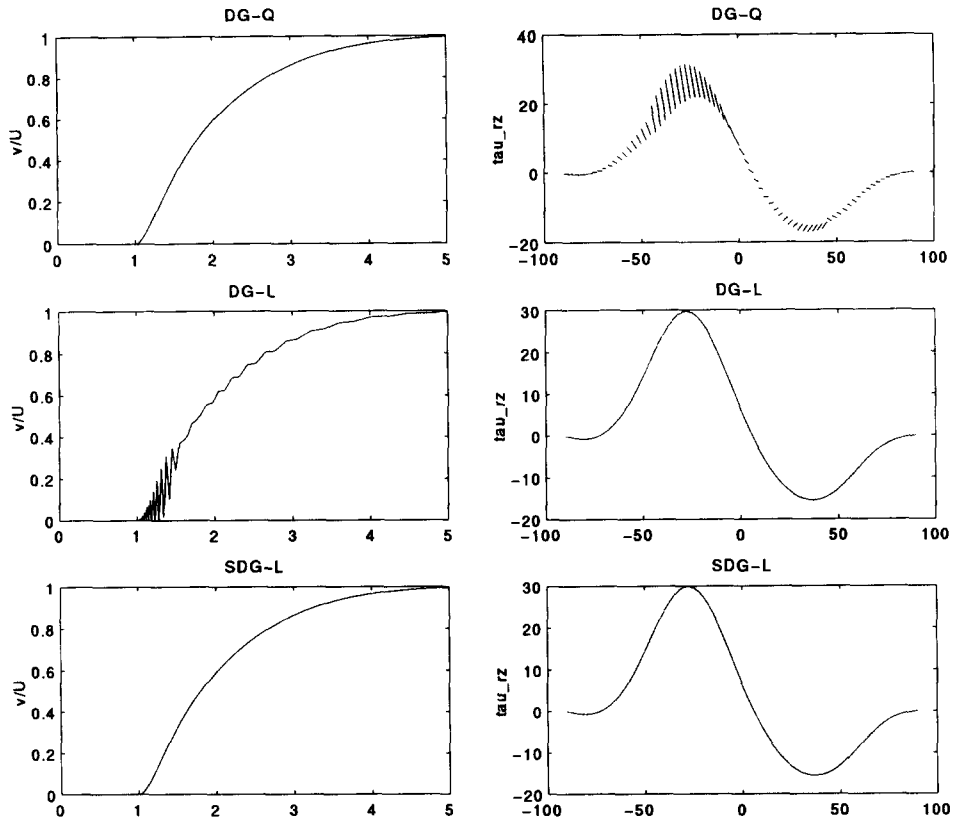

Fig. 9. Falling sphere in a tube (UCM model, De = 0.8, mesh M4): left, discontinuous τ_{rz} on surface of the sphere (from upstream to downstream); right, velocity on centre-line downstream; top, DG–E method; middle, DG–E method using bilinear discretization for extra stress; bottom, DG–SE method.

giving a combination of the lower and upper convected derivative (Table 6). For the Giesekus model, $\xi = 0$. Fig. 12 demonstrates the quality of the fit of the complex moduli, while Fig. 13 shows the fit of the viscosity and first normal stress difference together with the predicted elongational viscosities. In this case only the four-mode models are shown. Remarkably, both PTT parameter sets exhibit a nearly equally good fit to the data. Model predictions of the elongational viscosity differ significantly.

The stress optical coefficient was determined in fully developed flow by comparing birefringence measurements with computed shear stresses. By application of Eq. (18) the stress optical coefficient was determined to be 1.3×10^9 Pa^{-1}.

6. Results

6.1. Flow around a symmetrically confined cylinder

Experiments are carried out at a temperature of 190°C. The average velocity is denoted by V, and the Deborah number is defined as

$$De = \frac{\bar{\lambda} V}{R}, \tag{19}$$

with

Fig. 10. Photograph of the flow cell.

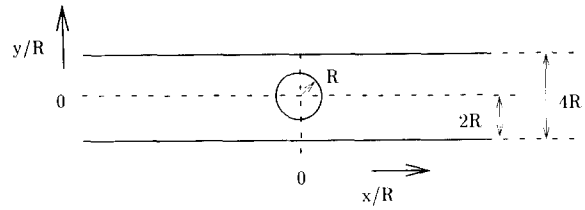

Fig. 11. Flow domain of the symmetrically placed cylinder.

$$\bar{\lambda} = \frac{\sum_{i=1}^{N} \eta_i \lambda_i}{\sum_{i=1}^{N} \eta_i}, \tag{20}$$

which is a viscosity-weighted average Maxwell relaxation time. Unless specified otherwise, the four-mode fit is applied. In the analysis the $(\tau, \boldsymbol{u}, p, \bar{\boldsymbol{D}}) \rightarrow (Q_1^d Q_2 P_1^d Q_1)$ element is used, while the auxiliary viscosity $\bar{\eta}$ is set to

$$\bar{\eta} = \sum_{i=1}^{N} \eta_i. \tag{21}$$

Two mean velocities are investigated: 8.06×10^{-3} m s^{-1} and 14.9×10^{-3} m s^{-1}, resulting in Deborah numbers of 4.4 and 8.1 respectively. Fig. 14 depicts the mesh near the cylinder. The mesh has an upstream length of $15R$, a downstream length of $20R$ and contains 1130 elements.

In Fig. 15 ($De = 4.4$) and Fig. 16 ($De = 8.1$) a comparison is made between experimental and computed isochromatic lines.

De = 4.4. At first sight all three computations agree reasonably well with the experimental isochromatic pattern. The Giesekus model appears to give the best prediction of the birefringent

Table 3
List of elements used in the polariscope

Device	Manufacturer	Part number
Polarizer	Meadowlark optics	DPM1.5HN38 s
$\lambda/4$ plate	Meadowlark optics	NQM1.5546
Interference filter, 546 nm	Spindler and Hoyer	37.1105
Mercury lamp	Philips	

Table 4
Characteristics of low density polyethylene used

Melt index (ISO 113 (A/4))	M_n	M_w	M_z	ρ (kg m^{-3}) (ISO 1183 (A))	T_c (°C)
8	1.3×10^4	1.55×10^5	7.8×10^5	9.2×10^2	98.6

M_n, number-averaged molecular weight; M_w, weight-average molecular weight; M_z, z-averaged molecular weight; ρ, density; T_c, crystallization temperature.

Table 5
Maxwell parameter values for four-mode and eight-mode fits low density polyethylene for melt at $T = 190°C$

Four-mode fit			Eight-mode fit		
η_i (Pa s)	λ_i (s)	η_s (Pa s)	η_i (Pa s)	λ_i (s)	η_s (Pa s)
8.50×10^0	3.16×10^{-5}	0.0	9.28×10^0	4.28×10^{-5}	0.0
1.37×10^2	1.00×10^{-3}		1.90×10^1	2.07×10^{-4}	
6.60×10^2	3.16×10^{-2}		7.21×10^1	1.30×10^{-3}	
1.65×10^3	1.00×10^0		2.20×10^2	9.00×10^{-3}	
			5.07×10^2	5.69×10^{-2}	
			8.25×10^2	3.50×10^{-1}	
			5.84×10^2	1.82×10^0	
			1.23×10^2	9.94×10^0	

Table 6
Parameter values for non-linear viscoelastic constitutive models for low density polyethylene melt at $T = 190°C$

Model	α	ξ	ε
PTT set 1	—	0.1	0.1
PTT set 2	—	0.0	0.2
Giesekus	0.25	—	

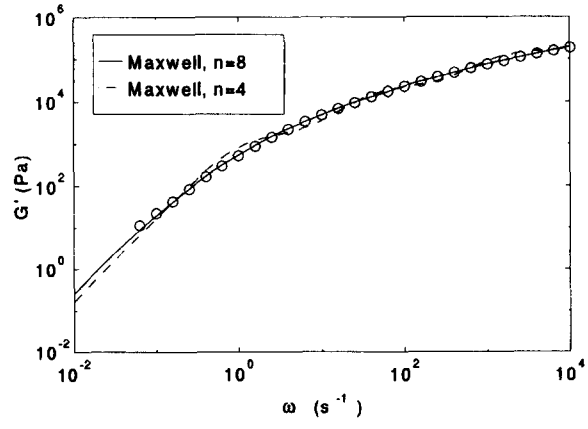

Fig. 12. Rheological data for LDPE melt at $T = 190°C$: complex modulus with fitted Maxwell models.

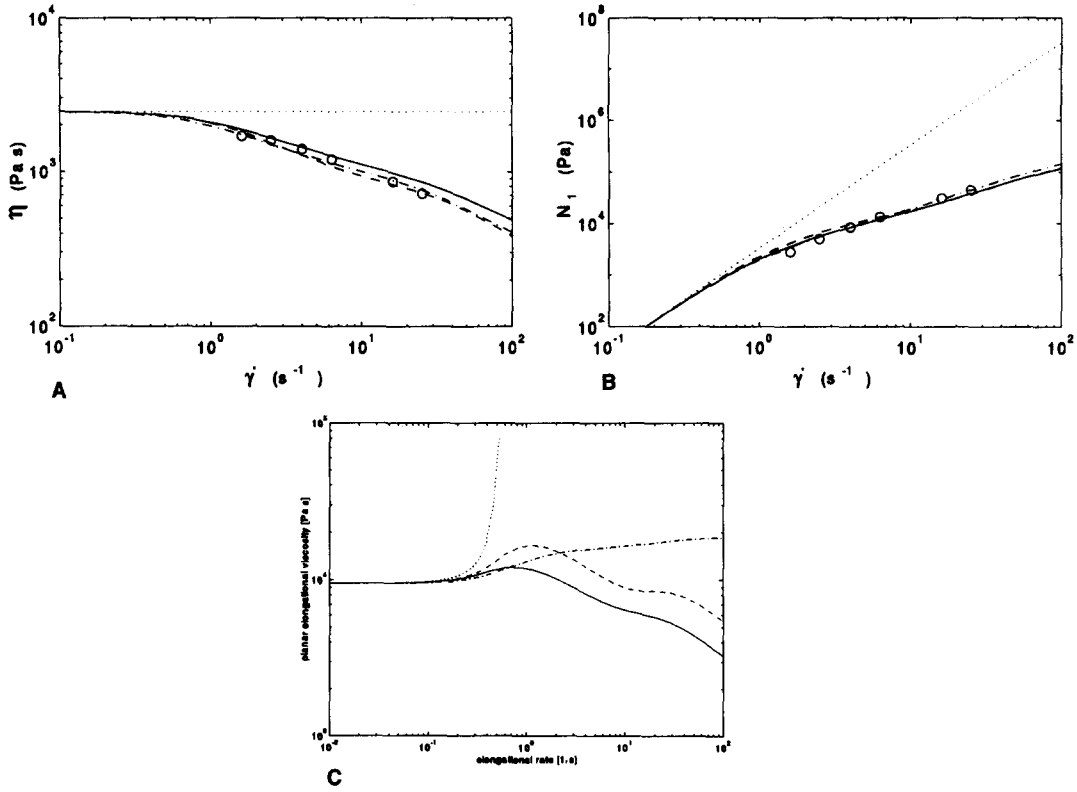

Fig. 13. Material functions for LDPE at 190°C in steady simple shear flow ((a) viscosity $\eta(\dot{\gamma})$; (b) first normal stress difference $N_1(\dot{\gamma})$) together with fitted models and (c) predictions in the steady planar elongational flow (—, PTT model with $\xi = 0.0$ and $\varepsilon = 0.2$; —— ——, PTT model with $\xi = 0.1$ and $\epsilon = 0.1$; – · –, Giesekus model; ···, UCM model).

tail at the wake of the cylinder. The PTT set 2 ($\xi = 0$, $\varepsilon = 0.2$) performs the poorest while PTT set 1 ($\xi = 0.1$, $\varepsilon = 0.1$) is intermediate between these two. Fig. 17 shows the predicted first normal stress difference N_1 along the centre-line. These results are consistent with the differences in the elongational behaviour of the three parameter sets. The maximum elongational rate along the downstream centre-line is approximately 10 s^{-1}. Furthermore, it can be seen that, unlike the

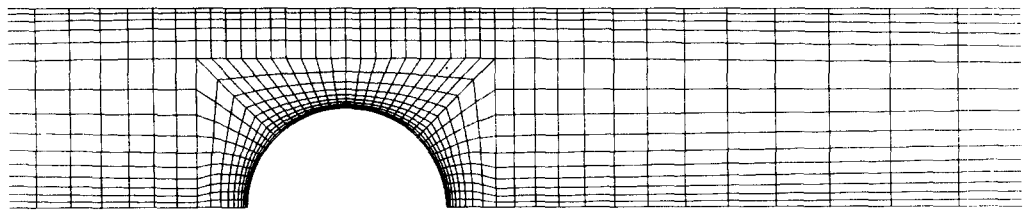

Fig. 14. Part of finite element method mesh for the symmetric confined cylinder used for the analysis of LDPE melt flow.

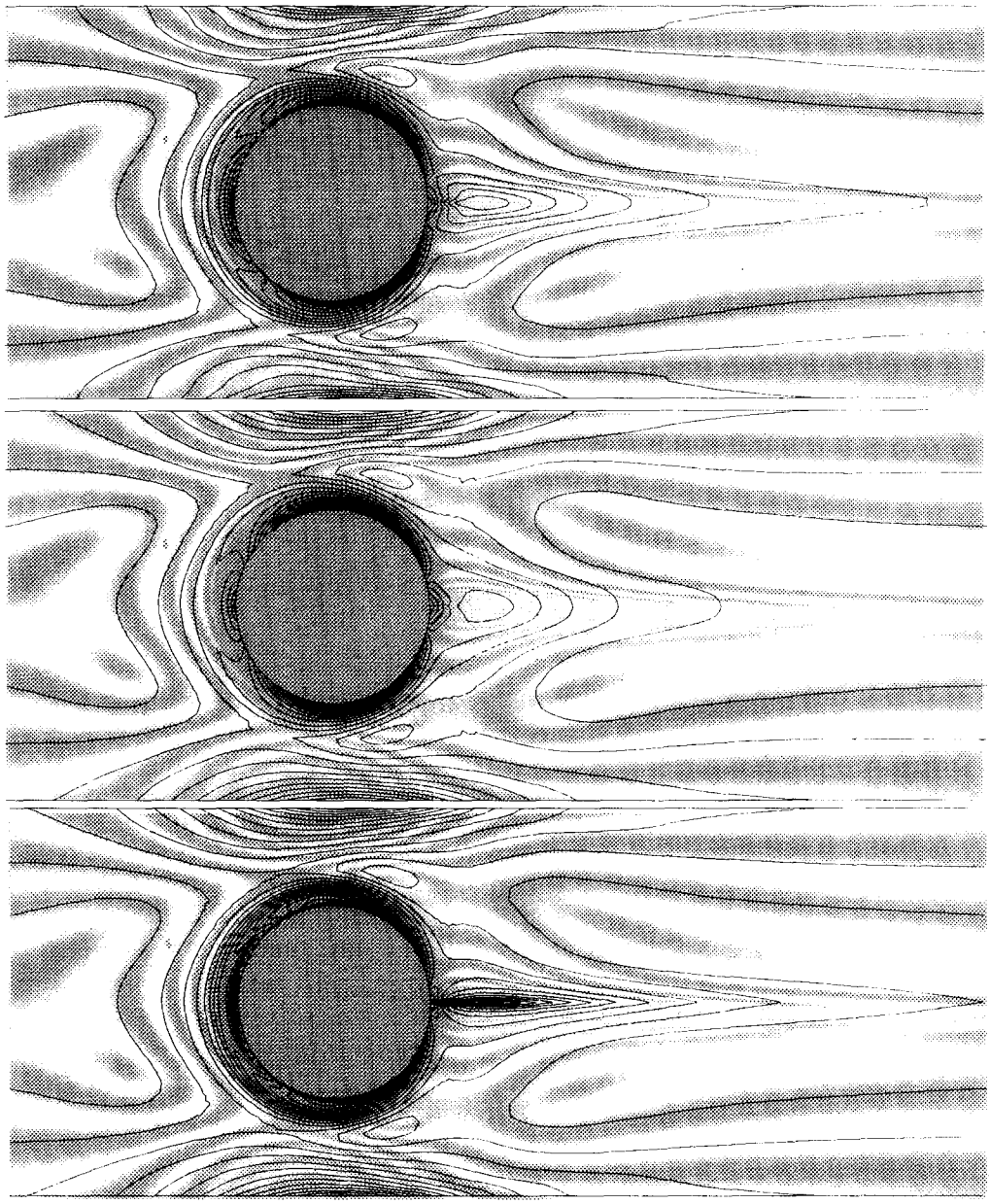

Fig. 15. Experimental and computed (——) isochromatic patterns at De = 4.4 for the symmetrically confined cylinder in a plane channel of LDPE melt at 190°C (flow from left to right). From top to bottom: PTT model with $\xi = 0.1$ and $\varepsilon = 0.1$; PTT model with $\xi = 0.0$ and $\varepsilon = 0.2$; Giesekus model with $\alpha = 0.25$.

Giesekus model, both PTT parameter sets predict a vertical slope of the fringe lines at the centre-line, which is not observed in the experiment. The number of fringe lines between the cylinder and the walls is over-predicted by all models. Parameter set 1 for the PTT model

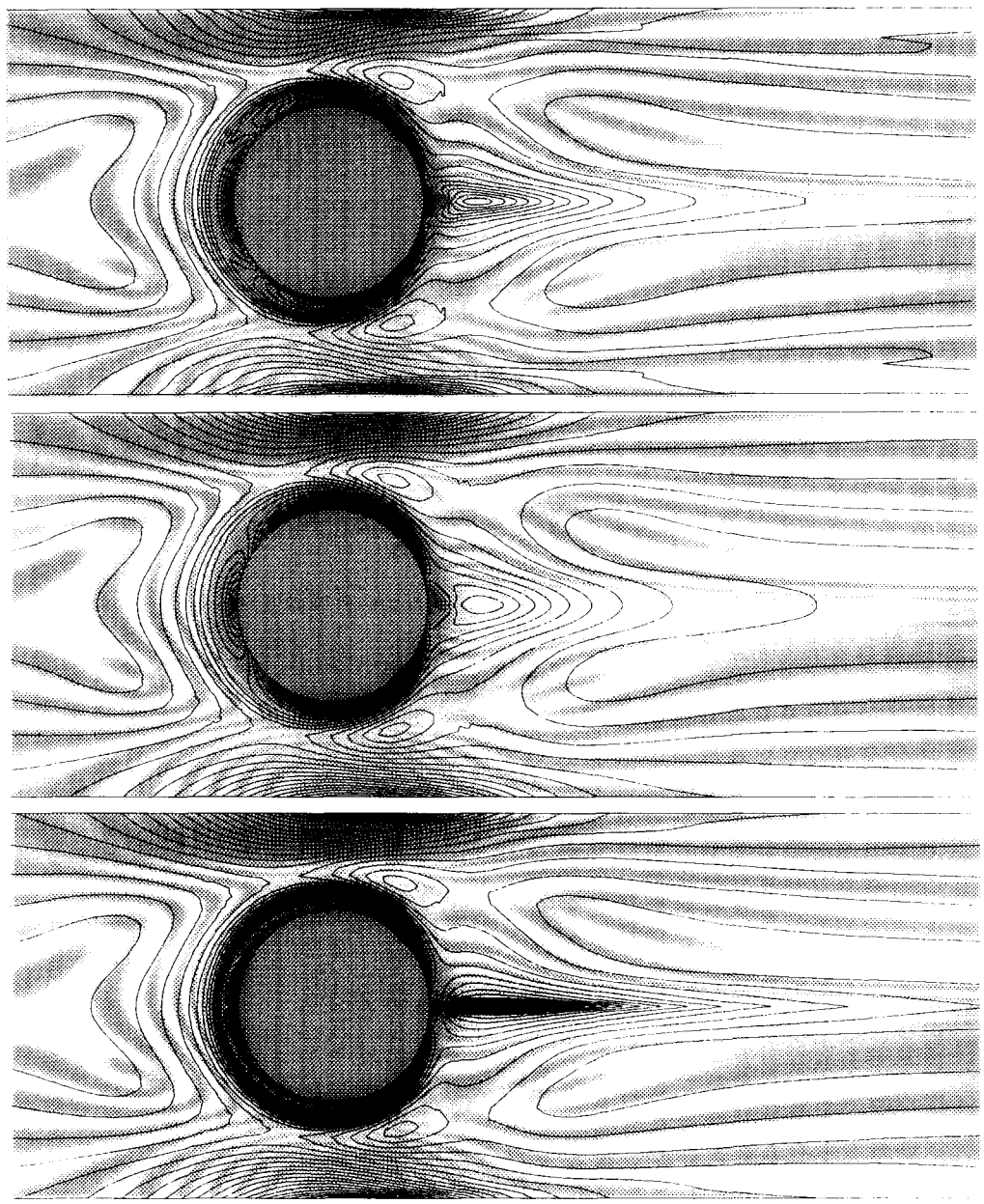

Fig. 16. Experimental and computed (——) isochromatic patterns at De = 8.1 for the symmetrically confined cylinder in a plane channel of LDPE melt at 190°C (flow from left to right). From top to bottom: PTT model with $\xi = 0.1$ and $\varepsilon = 0.1$; PTT model with $\xi = 0.0$ and $\varepsilon = 0.2$; Giesekus model with $\alpha = 0.25$.

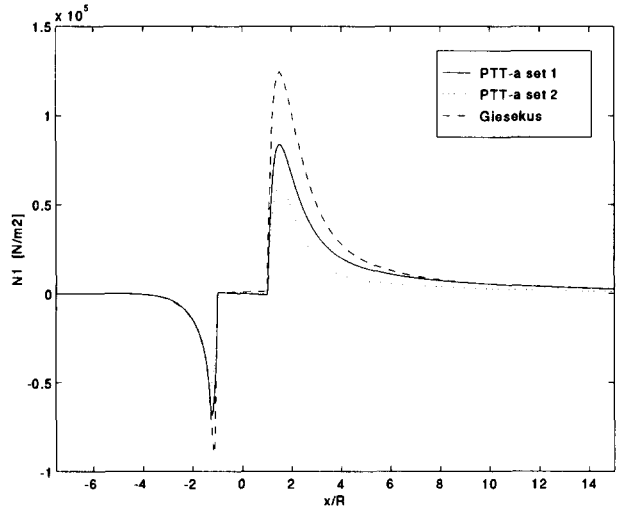

Fig. 17. Computed first normal stress difference along the centre-line at De = 4.4 for symmetrically confined cylinder in a plane channel of LDPE melt at 190°C.

performs best in this respect. The computed maximum wall shear rate is 83 s^{-1}, which is unfortunately outside the measurement range of the steady shear data; see Fig. 13.

The isochromatic lines near the surface of the cylinder could not be resolved in the experiment as they are in the shade of the cylinder.

De = 8.1. At a Deborah number of 8.1 similar behaviour is observed to that for *De* = 4.4. The maximum shear rate at the boundary opposite to the cylinder is approximately 150 s^{-1}. The top of the photograph is not clear owing to reflection in the wall of the flow cell.

6.2. *Asymmetrically confined cylinder*

In this case, the cylinder is moved 0.3*R* towards the upper wall. Part of the mesh is given in Fig. 18; it extends 10*R* upstream and 15*R* downstream and has 2024 elements.

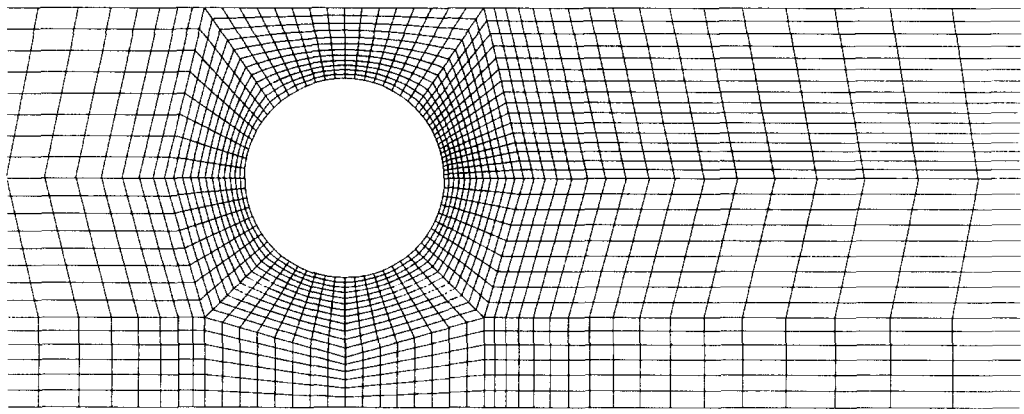

Fig. 18. Part of finite element mesh for the asymmetric confined cylinder used for the analysis of LDPE melt flow.

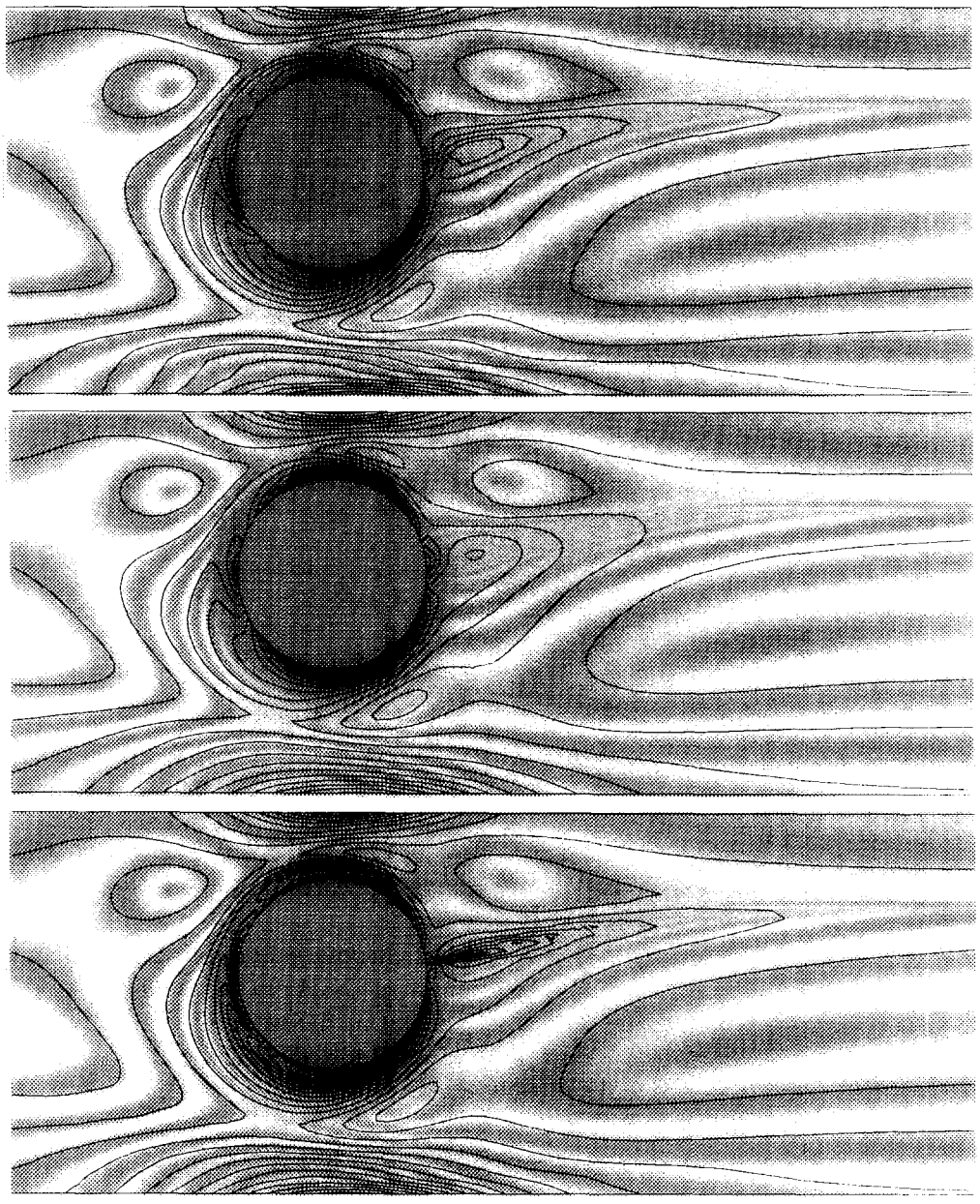

Fig. 19. Experimental and computed (——) isochromatic patterns at $De = 4.6$ for the asymmetrically placed cylinder in a plane channel of LDPE melt at 190°C (flow from left to right). From top to bottom: PTT model with $\xi = 0.1$ and $\varepsilon = 0.1$; PTT model with $\xi = 0.0$ and $\varepsilon = 0.2$; Giesekus model with $\alpha = 0.25$.

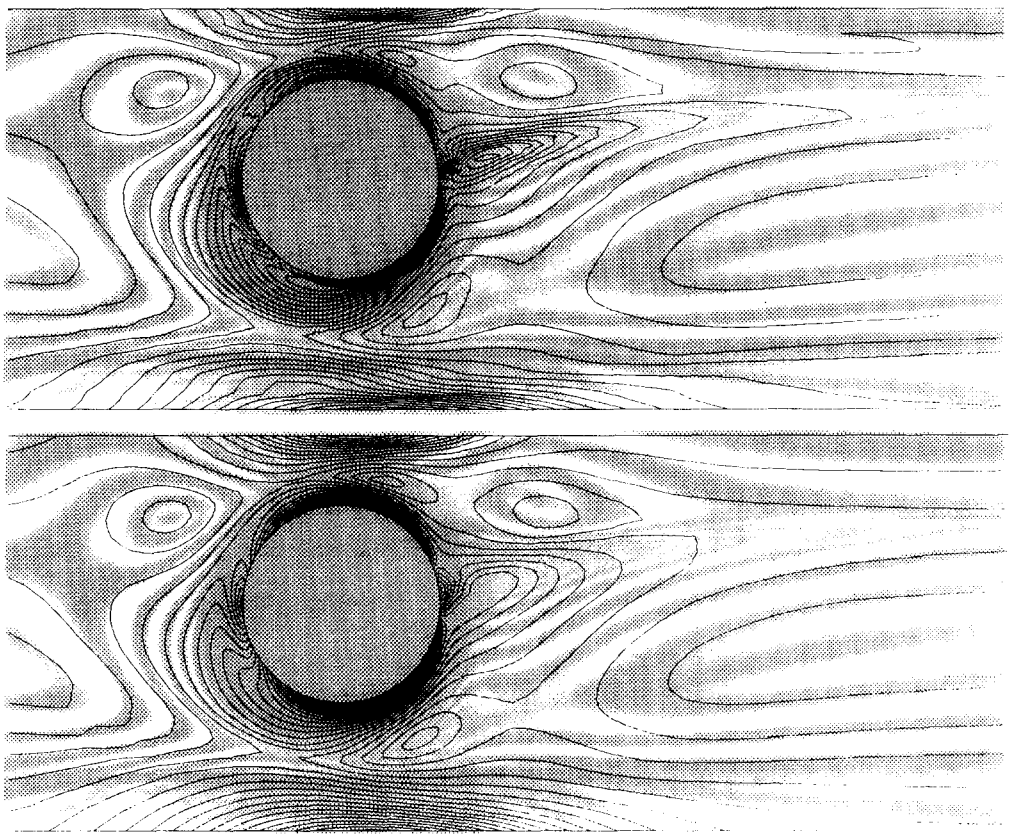

Fig. 20. Experimental and computed (——) isochromatic patterns at $De = 8.9$ for the asymmetrically placed cylinder in a plane channel of LDPE melt at 190°C (flow from left to right). From top to bottom: PTT model with $\xi = 0.1$ and $\varepsilon = 0.1$; PTT model with $\xi = 0.0$ and $\varepsilon = 0.2$.

Again two mean velocities were used in the experiments and computations 8.53×10^{-3} m s^{-1} and 16.4×10^{-3} m s^{-1}, resulting in Deborah numbers of respectively 4.6 and 8.9. In Fig. 19 ($De = 4.6$) and Fig. 20 ($De = 8.9$) a comparison is made between the experimental and computed isochromatic lines.

De = 4.6. A good agreement is found between the isochromatic lines of the experiment and the computations using PTT set 1 ($\xi = 0.1$, $\varepsilon = 0.1$) and Giesekus. As in the symmetric case the PTT set 2 ($\xi = 0$, $\varepsilon = 0.2$) computation fails to predict the tail in the wake of the cylinder. Problems with observing lines near the cylinder are the same as reported with the symmetric flow.

De = 8.9. For this case the computation using the Giesekus model failed owing to divergence of the iteration process, while for parameter sets 1 and 2 the same conclusions can be drawn as for the lower Deborah number, although the agreement is less good.

6.3. Parameter variation

To investigate the influence of the material parameters in the constitutive models, a parameter variation has been performed. All these computations were done using the symmetrical

geometry and the low mean velocity ($U = 8.06 \times 10^{-3}$ m s^{-1}). First, the non-linear parameters ξ, ε and α are varied using the four-mode fit.

In Fig. 21 the results of the computation of the isochromatic lines using the PTT model are depicted. The non-linear parameters are varied from ($\xi = 0.0, \varepsilon = 0.2$) via ($\xi = 0.05, \varepsilon = 0.15$) and ($\xi = 0.1, \varepsilon = 0.01$) to ($\xi = 0.15, \varepsilon = 0.05$). These parameter sets have been chosen such that steady shear data are still predicted correctly. Yet, significant differences in the predicted steady planar elongational flow properties are observed (see Fig. 22).

Increasing the parameter ξ and decreasing the parameter ε has a positive effect on the prediction of the tail in the wake of the cylinder, which is a consequence of the increased elongational viscosity seen in Fig. 22. If ξ is chosen too large, it has a negative effect on the smoothness of the predicted stress distribution. This is also reflected in the failure to achieve convergence with $\xi = 0.2$ and $\varepsilon = 0.0$.

In Fig. 23 the results of the computation of the isochromatic lines using the Giesekus model are shown. The parameter α is varied from 0.15 via 0.25 to 0.35. Again, these parameters have their influence on steady planar elongational flow predictions (Fig. 24) and, consequently, on the predictions of the tail as well. The influence on the steady shear behaviour is relatively small, but larger than the changes observed for the PTT model. The number of fringe lines between the cylinder and the walls, and in the wake of the cylinder, tends to increase with decreasing α.

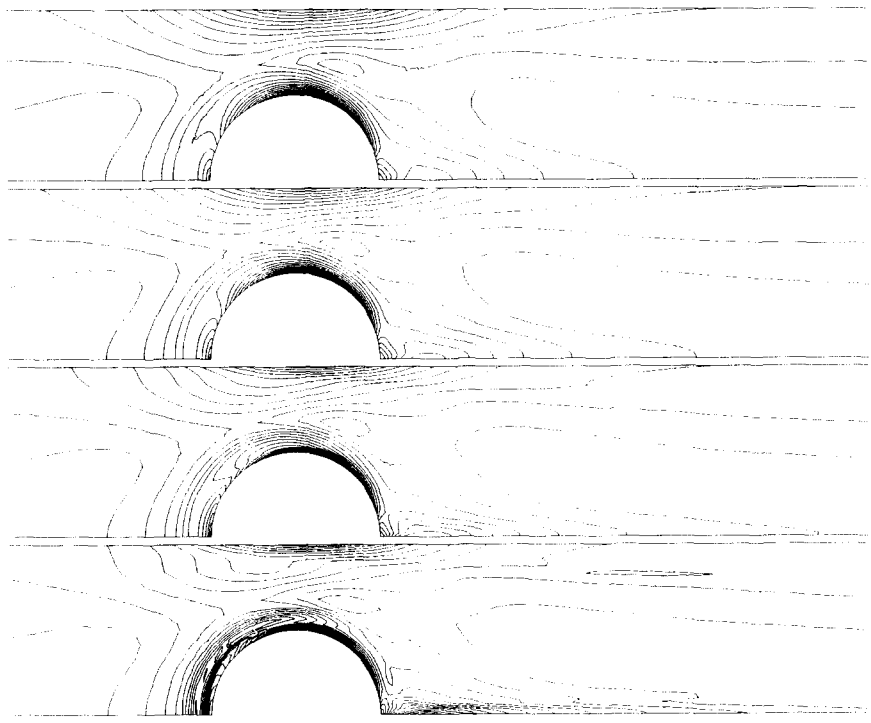

Fig. 21. Computed isochromatic patterns at $De = 4.4$ for the cylinder placed symmetrically in a plane channel of LDPE melt at 190°C (flow from left to right). From top to bottom: PTT-a model with $\xi = 0.0$ and $\varepsilon = 0.2$, $\xi = 0.05$ and $\epsilon = 0.15$, $\xi = 0.1$ and $\epsilon = 0.1$, $\xi = 0.15$ and $\epsilon = 0.05$.

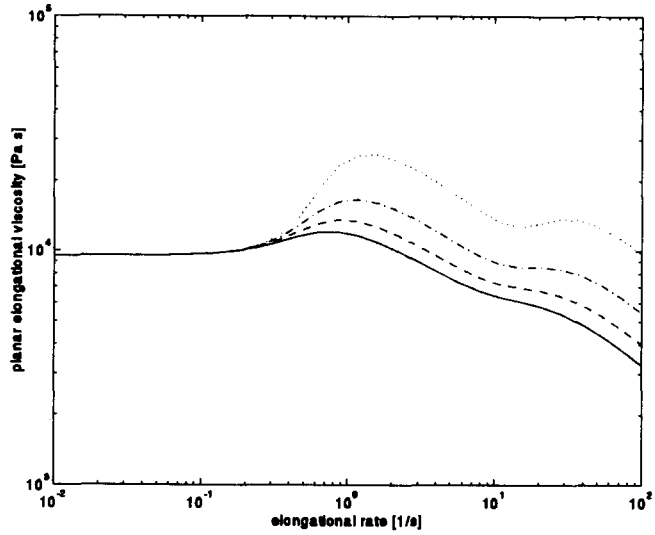

Fig. 22. Predictions using PTT model (four-mode) in steady planar elongational flow for LDPE at 190°C: ——, $\xi = 0.0$ and $\varepsilon = 0.2$; —— ——, $\xi = 0.05$ and $\varepsilon = 0.15$; – · –, $\xi = 0.1$ and $\varepsilon = 0.1$; ···, $\xi = 0.15$ and $\varepsilon = 0.05$.

Finally, the influence of the number of relaxation times is investigated. The computations were performed using the PTT model with $\xi = 0.1$ and $\varepsilon = 0.1$. A one-mode, a four-mode and an eight-mode fit are used. In case of the one-mode fit $\eta = 1.6 \times 10^3$ Pa s, $\lambda = 0.15$ s, while a non-zero newtonian contribution is used: $\eta_s = 0.4 \times 10^3$ Pa s. The result of the computations of the isochromatic lines is presented in Fig. 25. The one-mode computation gives an isochromatic pattern that looks similar to the pattern using the four-mode fit, but many details are lost.

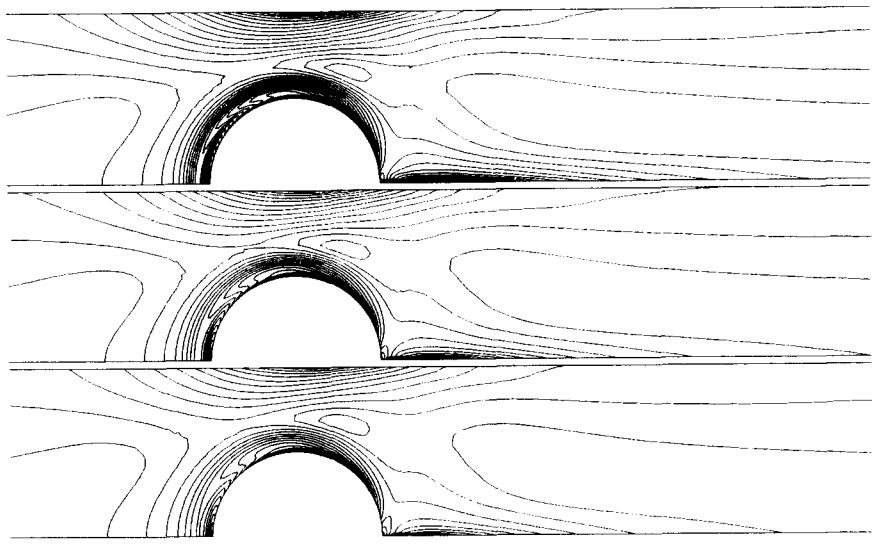

Fig. 23. Computed isochromatic patterns at De = 4.4 for the cylinder placed symmetrically in a plane channel of LDPE melt at 190°C (flow from left to right). From top to bottom: Giesekus model with $\alpha = 0.15$, $\alpha = 0.25$, $\alpha = 0.35$.

Generally speaking, adding more modes improves details. See for instance the position of the island above the cylinder. The difference between the four-mode and eight-mode result is small; only little details change. In particular, the isochromatic lines near the wall tend to become smoother. In Fig. 26 the velocity in the flow direction along the centre-line is given. Here, differences between all three computations are small.

Selection of the distribution and number of the relaxation times depends on the flow regime analysed. To each relaxation time λ_i, a Deborah number may be associated: $De_i = \lambda_i V/R$. If this Deborah number is sufficiently small, this particular mode may generally effectively be modelled as a purely viscous contribution. Furthermore, in the computations the number of relaxation times may be increased until no significant change in the solution is noticed.

7. Conclusions

In this study, the planar flow of an LDPE melt at 190°C past a cylinder, placed between two parallel plates, has been investigated to test the performance of two constitutive models: the exponential version of the PTT model and the Giesekus model. Evaluation is based on the comparison of measured and computed isochromatic fringes. For the symmetrically confined cylinder the Deborah numbers studied are 4.4 and 8.1, while for the asymmetrically placed cylinder the Deborah numbers used are 4.6 and 8.9. The main conclusions can be summarized as follows.

7.1. Numerical method

An enhancement of the DG method is proposed, based on the results of Guénette and Fortin [24]. The new method is labelled DG–SE, to emphasize the enhanced stability (S) of the method

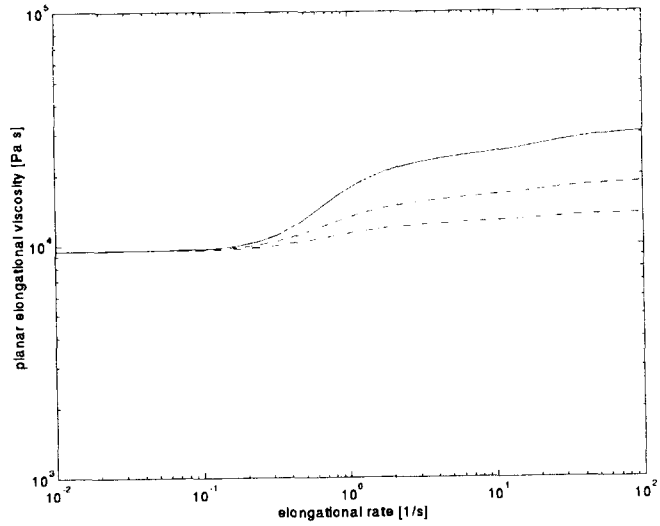

Fig. 24. Predictions using the Giesekus model (four-mode) in steady planar elongational flow for LDPE at 190°C: ——, $\alpha = 0.15$; —— ——, $\alpha = 0.25$, – · –, $\alpha = 0.35$.

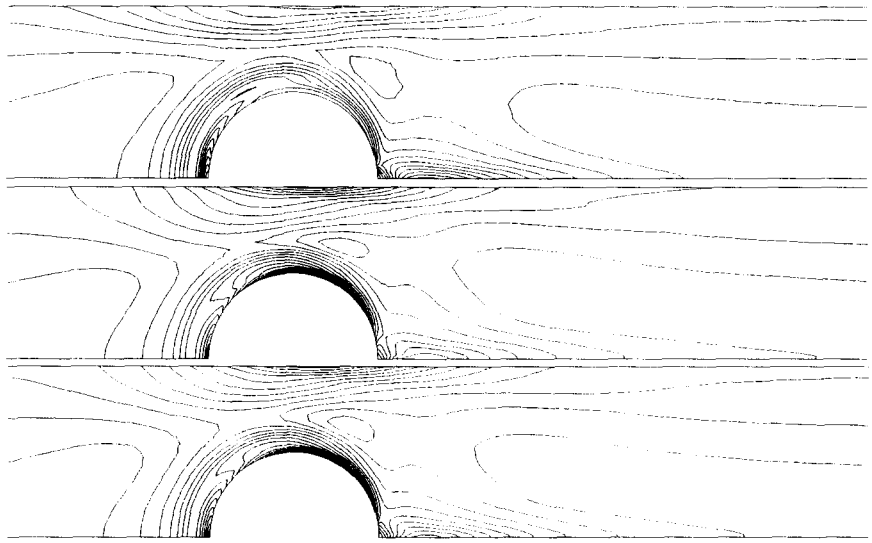

Fig. 25. Computed isochromatic patterns at $De = 4.4$ for the cylinder placed asymmetrically in a plane channel of LDPE melt at 190°C (flow from left to right). From top to bottom PTT model with $\xi = 0.1$ and $\varepsilon = 0.1$: one-mode fit, four-mode fit, eight-mode fit.

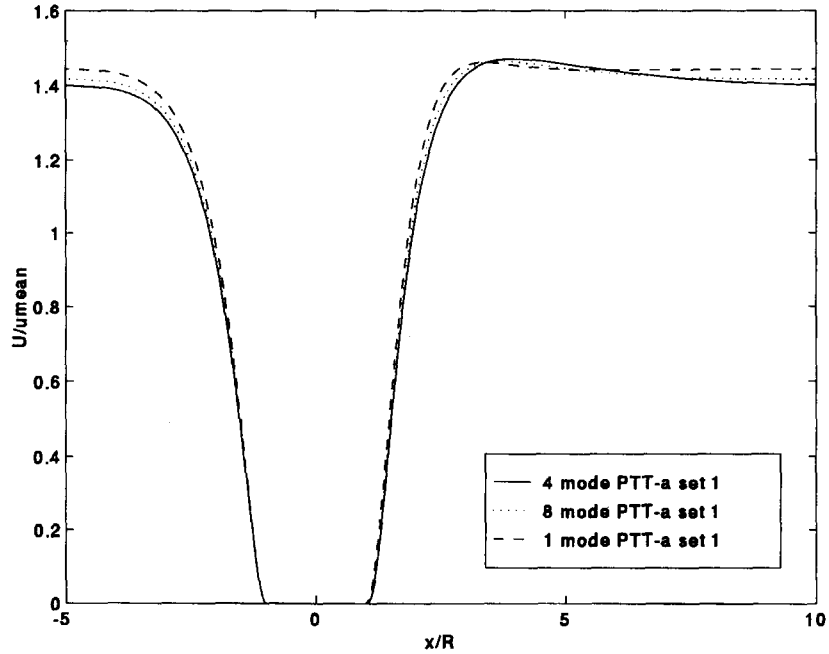

Fig. 26. Velocity along the centre-line using PTT model (set 1) with the one-, four- and eight-mode Maxwell fits.

and the explicit (E) approximation of certain terms in the integrand involving neighbouring elements. This explicit approximation was first introduced elsewhere [26] and allows the efficient resolution of problems with multiple relaxation times, because the majority of the degrees of freedom (extra stresses) can be eliminated on the element level. Consequently, the computing time is approximately linearly proportional to the number of relaxation times. The enhanced stability is manifested in the increased value of the Deborah number (2.7) at which convergence is obtained for the falling sphere in a tube benchmark problem using a UCM fluid. The best performance, in this respect, is achieved with the bilinear stress element with a bilinear continuous approximation of the rate of strain tensor: $(\boldsymbol{\tau}, \boldsymbol{u}, p, \bar{\boldsymbol{D}}) \rightarrow (Q_1^d Q_2 P_1^d Q_1)$. Further work is needed to find the optimal choice of the auxiliary viscosity $\bar{\eta}$.

7.2. Experimental results

Based on viscometric shear flow data only, no distinction can be made between the three different sets for the non-linear parameters $(\xi, \varepsilon, \alpha)$ of the PTT and the Giesekus model. All fits show an equally good fit of the available data $[\eta(\dot{\gamma}), N_1(\dot{\gamma})]$. For instance for the PTT model the shear properties are relatively insensitive to variations in ξ and ε. This in contrast with the (planar) elongational viscosity. Consequently, the prediction of the birefringence profiles in the wake of the cylinder, which is dominated by elongational properties, is sensitive to the choice of these non-linear parameters. Neither of the models proved to be able to predict the full birefringence distribution correctly. PTT set 2 ($\xi = 0$, $\varepsilon = 0.1$) provides the poorest prediction: it predicts far too few fringe lines in the wake of the cylinder. The Giesekus model seems to capture the birefringent tail best, but experimental resolution of this tail is limited, as fringes are packed closely. The PTT set 1 ($\xi = 0.1$, $\varepsilon = 0.1$) appears to give the best overall prediction. In particular the shape and number of fringes between the wall and the cylinder is predicted better than with the Giesekus model. This is best illustrated at the higher Deobrah number and for the asymmetrically placed cylinder.

Both the PTT and the Giesekus model have difficulty in predicting the combined shear–elongational flow between the cylinder and the walls. This suggests that, even if elongational properties are available, this would still be insufficient to characterize fully the material. Moreover, constitutive models like the PTT and the Giesekus model may prove inadequate to predict complex flows, and more refined models appear to be necessary.

If material parameters cannot be fully identified by viscometric shear and elongational data only, complex flow data should be included in the characterization procedure. This can be achieved by comparing numerical and experimental results to optimize material parameters. An example of such a procedure may be found in [38].

Compared with similar work on polymer solutions [1], the current study has some limitations: velocities have not been measured yet and the fringe patterns are only semiquantitative, compared with pointwise birefringence measurements using, for instance, the ROA developed by Fuller and Mikkelsen [4]. The mean velocity used for polymer solutions is an order of magnitude higher than for polymer melts, allowing the application of existing LDA technology. For polymer melts particle tracking velocimetry appears to be a more versatile approach and is currently under construction.

Acknowledgements

We gratefully acknowledge Toon van Gils and Sjef Garenfeld for constructing parts of the experimental apparatus and Peter Kruijt for his contribution to the experiments.

References

[1] J.H.W. Baaijens, G.W.M. Peters, F.P.T. Baaijens and H.E.H. Meijer, Viscoelastic flow past a confined cylinder of a polyisobutylene solution, J. Rheol., 39 (1995) 1243–1277.
[2] K. Walters, Recent developments in rheometry. In P. Moldenears and R. Keunings (eds.), Proc. XI Int. Cong. on Rheology, Elsevier, Amsterdam, 1992, pp. 16–23.
[3] N.E. Hudson and T.E.R. Jones, the A1 project, an overview. J. Non-Newtonian Fluid Mech., 46 (1993) 69–88.
[4] G.G. Fuller and K.J. Mikkelsen, Note: optical rheometry using a rotary polarization modulator, J. Rheol., 33 (1989) 761–769.
[5] S.T.E. Aldhouse, M.R. Mackley and I.P.T. Moore, Experimental and linear viscoelastic stress distribution measurement of high density polyethylene flowing into and within a slit. J. Non-Newtonian Fluid Mech., 21 (1986) 359–376.
[6] C.D. Han and L.H. Drexler, Studies of converging flows of viscoelastic polymeric melts, (i) stress birefringent measurements in the entrance region of a sharp-edged slit die, J. Appl. Polym. Sci., 17 (1973) 2329–2354.
[7] C.D. Han and L.H. Drexler, Studies of converging flows of viscoelastic polymeric melts, (ii) stress and velocity distributions in the entrance region of a sharp-edged slit die, J. Appl. Polym. Sci., 17 (1973) 2355–2368.
[8] C.D. Han and L.H. Drexler, Studies of converging flows of viscoelastic polymeric melts, (iii) velocity measurement in the entrance region of a sharp-edged slit die, J. Appl. Polym. Sci., 17 (1973) 2369–2393.
[9] A.I. Isayev and R.K. Upadhyay, Two-dimensional viscoelastic flows: experimentation and modeling, J. Non-Newtonian Fluid Mech., 19 (1985) 135–160.
[10] T. Kajiwara, S. Nonomiya, Y. Kuwano and K. Funatsu, Numerical simulation of converging flow of polymer melts through a tapered slit die. J. Non-Newtonian Fluid Mech., 48 (1993) 111–124.
[11] D.G. Kiriakidis, H.J. Park, E. Mitsoulis, B. Vergnes and J.F. Agassant, A study of stress distribution in contraction flows of a LLDPE melt, J. Non-Newtonian Fluid Mech., 47 (1993) 847–874.
[12] H. Maders, B.F. Vergnes, Y. Demay and J.F. Agassant, Steady flow of a White–Metzner fluid in a 2d abrupt contraction: computation and experiments, J. Non-Newtonian Fluid Mech., 45 (1992) 63–80.
[13] S.A. White and D.G. Baird, Flow visualization and birefringence studies on planar entry flow of polymer melts, J. Non-Newtonian Fluid Mech., 30 (1988) 47–71.
[14] R. Ahmed and M.R. Mackley, Experimental centreline planar extension of polyethylene melt flowing into a slit die. J. Non-Newtonian Fluid Mech., 56 (1995) 127–149.
[15] R. Ahmed, R. Liang and M.R. Mackley, The experimental observation and numerical prediction of planar entry flow and die swell for molten polyethylene, J. Non-Newtonian Fluid Mech., 59 (1995) 129–153.
[16] C. Beraudo, Methodes elements finis pour la simulation numerique d'ecoulement de fluides viscoelastiques de type differentiel dans de geometries convergentes, Ph.D. Thesis, CEMEF, 1995.
[17] R.A. Brown and G.H. McKinley, Report on the 8th international workshop on numerical methods in viscoelastic flows, J. Non-Newtonian Fluid Mech., 52 (1994) 407–413.
[18] S. Dupont and M. Crochet, The vortex growth of a KBKZ fluid in an abrupt contraction, J. Non-Newtonian Fluid Mech., 29 (1988) 81–91.
[19] X.L. Luo and E. Mitsoulis, A numerical study of the effect of elongational viscosity on vortex growth in contraction flows of polyethylene melts. J. Rheol., 34 (1990) 309.
[20] M.A. Hulsen and J. van der Zanden, Numerical simulation of contraction flows using a multi-mode Giesekus model, J. Non-Newtonian Fluid Mech., 38 (1991) 183–221.
[21] F.P.T. Baaijens, Numerical analysis of start-up planar and axisymmetric contraction flows using multi-mode differential constitutive models, J. Non-Newtonian Fluid Mech., 48 (1993) 147–180.

[22] D. Rajagopalan, R.C. Armstrong and R.A. Brown, Finite element methods for calculation of steady viscoelastic flow using constitutive equations with a newtonian viscosity, J. Non-Newtonian Fluid Mech., 26 (1990) 159–192.
[23] M. Fortin and A. Fortin, A new approach for the FEM simulation of viscoelastic flows, J. Non-Newtonian Fluid Mech., 32 (1989) 295–310.
[24] R. Guénette and M. Fortin, A new mixed finite element method for computing viscoelastic flows, J. Non-Newtonian Fluid Mech., 60 (1995) 27–52.
[25] F.P.T. Baaijens, H.P.W. Baaijens, G.W.M. Peters and H.E.H. Meijer, An experimental and numerical investigation of a viscoelastic flow around a cylinder, J. Rheol., 38 (1994) 351–376.
[26] F.P.T. Baaijens, Numerical experiments with a discontinuous Galerkin method including monotonicity enforcement on the stick–slip problem, J. Non-Newtonian Fluid Mech., 51 (1994) 141–159.
[27] J.M. Marchal and M.J. Crochet, A new mixed finite element for calculating viscoelastic flow, J. Non-Newtonian Fluid Mech., 26 (1987) 77–114.
[28] F.P.T. Baaijens, Application of low-order discontinuous Galerkin methods to the analysis of viscoelastic flows, J. Non-Newtonian Fluid Mech., 52 (1994) 37–57.
[29] M.J. Szady, T.R. Salomon, A.W. Liu, D.E. Bornside, R.C. Armstrong and R.A. Brown, A new mixed finite element method for viscoelastic flows governed by differential constitutive equations, J. Non-Newtonian Fluid Mech., 59 (1995) 215–243.
[30] W.J. Lunsmann, L. Genieser, R.C. Armstrong and R.A. Brown, Finite element analysis of steady viscoelastic flow around a sphere in a tube: calculations with constant viscosity models, J. Non-Newtonian Fluid Mech., 48 (1993) 63–99.
[31] Y. Fan and M.J. Crochet, High-order finite element methods for steady viscoelastic flows, J. Non-Newtonian Fluid Mech., 57 (1995) 283–311.
[32] M.T. Argio, D. Rajagopalan, N. Shapley and G.H. McKinley, The sedimentation of a sphere through an elastic fluid, J. Non-Newtonian Fluid Mech., 60 (1995) 225–257.
[33] A. Kuske and G. Robertson, Photoelastic Stress Analysis, Wiley, London, 1977.
[34] M.E. Mackey and D.V. Boger, Flow Visualization in Rheometry, Elsevier, Amsterdam, 1988.
[35] G.G. Fuller, Optical rheometry, Annu. Rev. Fluid Mech., 22 (1990) 387–417.
[36] R.M.A. Azzam and N.M. Bashara, Ellipsometry and Polarized Light, North-Holland, Amsterdam, 1987.
[37] P. Tas, Film blowing: from polymer to product, Ph.D. Thesis, Eindhoven University of Technology, 1994.
[38] O. Op den Camp, Identification algorithms for time-dependent materials, Ph.D. Thesis, Eindhoven University of Technology, 1996.